From Beetles in Nature to the Laboratory: Actuating Underwater Locomotion on Hydrophobic Surfaces

Bat-El Pinchasik,*,[†] Jan Steinkühler,[‡] Pieter Wuytens,[§] Andre G. Skirtach,[§,‖] Peter Fratzl,[†] and Helmuth Möhwald[⊥]

[†]Department of Biomaterials, [‡]Department of Theory and Bio-systems, and [⊥]Emeritus Group of Interfaces, Max-Planck Institute of Colloids and Interfaces, Golm/Potsdam, D14476 Germany

[§]Photonics Research Group, IMEC, INTEC Department and [‖]Department of Molecular Biotechnology and NB-Photonics, Ghent University, 9000 Ghent, Belgium

Ⓢ *Supporting Information*

ABSTRACT: The controlled wetting and dewetting of surfaces is a primary mechanism used by beetles in nature, such as the ladybird and the leaf beetle for underwater locomotion.[1] Their adhesion to surfaces underwater is enabled through the attachment of bubbles trapped in their setae-covered legs. Locomotion, however, is performed by applying mechanical forces in order to move, attach, and detach the bubbles in a controlled manner. Under synthetic conditions, however, when a bubble is bound to a surface, it is nearly impossible to maneuver without the use of external stimuli. Thus, actuated wetting and dewetting of surfaces remain challenges. Here, electrowetting-on-dielectric (EWOD) is used for the manipulation of bubble−particle complexes on unpatterned surfaces. Bubbles nucleate on catalytic Janus disks adjacent to a hydrophobic surface. By changing the wettability of the surface through electrowetting, the bubbles show a variety of reactions, depending on the shape and periodicity of the electrical signal. Time-resolved (μs) imaging of bubble radial oscillations reveals possible mechanisms for the lateral mobility of bubbles on a surface under electrowetting: bubble instability is induced when electric pulses are carefully adjusted. This instability is used to control the surface-bound bubble locomotion and is described in terms of the change in surface energy. It is shown that a deterministic force applied normal can lead to a random walk of micrometer-sized bubbles by exploiting the phenomenon of contact angle hysteresis. Finally, bubble use in nature for underwater locomotion and the actuated bubble locomotion presented in this study are compared.
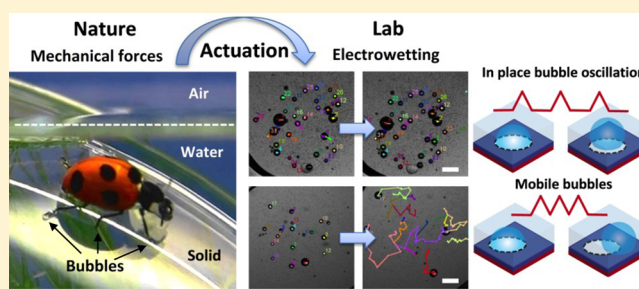
INTRODUCTION

Many plants in nature, especially the lotus leaf,[2] are famous for their ability to render droplets mobile on their surface.[3] Because of the superhydrophobic nature of these surfaces and minimal pinning,[4,5] a droplet reaching the surface easily rolls off, carrying contaminants on its way. Several attempts were made in the last few years to mimic such materials that induce droplet mobility on their surfaces.[6−9] In addition, the enhancement of droplet locomotion due to coalescence was recently reproduced with synthetic hierarchical structures.[10] However, an equivalent underwater propulsion mechanism of bubbles at the solid−water interface is missing, not without reason. Surface-bound bubbles are highly pinned and particularly challenging to render mobile. A key tool to tune the hydrophobic−hydrophilic interactions of droplets or bubbles with a surface is provided by materials with tunable wettability. Examples of such materials were previously reported using mostly UV irradiation.[11−13] Calculations show that electric fields can also be potentially used on superhydrophobic graphene surfaces.[14] However, these reversible transitions between hydrophobic and hydrophilic states are rather slow and involve changes in the surface

chemistry. In contrast, electrowetting shows rapid responses to applied electric voltage, modulating the hydrophobicity of dielectric materials.[15,16] Under applied voltage, the hydrophobicity drops, i.e., the contact angle decreases, rendering a hydrophobic surface more hydrophilic. Interestingly, electrowetting is also used for moving droplets and detaching them from hydrophobic surfaces, a fact that broadens the applicability of this method tremendously.[17−19] It was previously shown that alternating voltage decreases the contact angle hysteresis of droplets.[20] Another study extended the research on the mobility of droplets on superhydrophobic surfaces to hydrophobic surfaces by modulating the shape and periodicity of the applied electric signal.[21] Electrowetting can be also applied to bubbles, exploiting the same principle of tunable wettability.[22] Electrowetting of bubbles can be used for the trapping, transportation, and controlled release of particles underwater.[23−25] This principle was also successfully used to attract
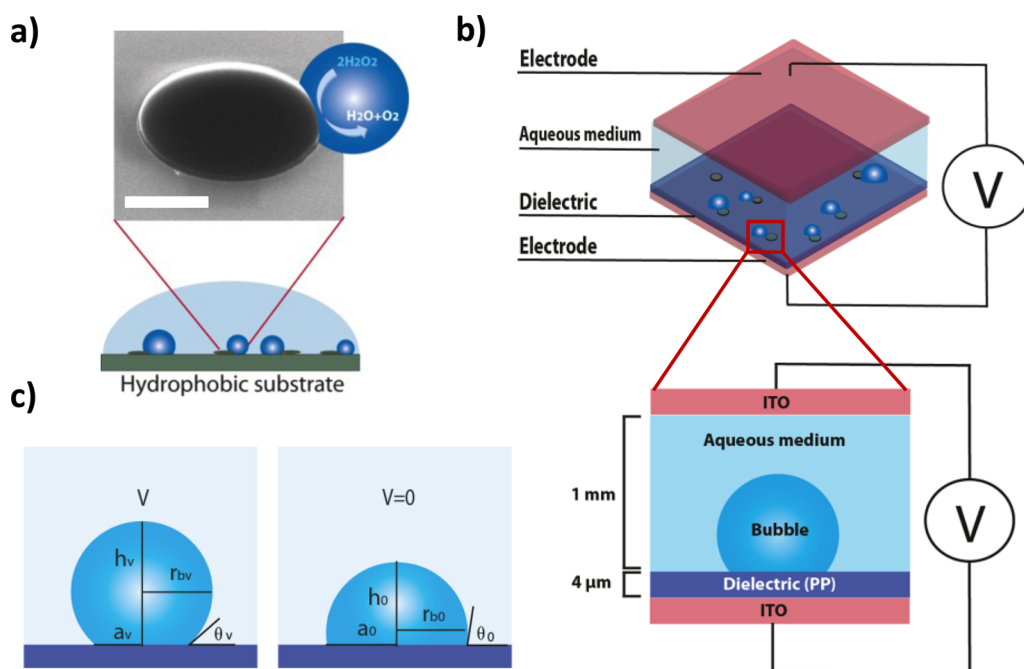
Figure 1. (a) Illustration of Janus disks dispersed on the solid–water interface, while bubbles nucleate on the catalytically active Pt side of the particles. (Inset) Scanning electron micrograph of a single Janus particle. The scale bar corresponds to 3 μm. (b) Illustration of the chamber designed for this study: bottom electrode (ITO), dielectric polypropylene layer, and upper electrode (ITO). The Janus disk–bubble complexes are distributed on the polypropylene layer. (c) Illustration showing the influence of a voltage on the wettability of the surface and consequently on the bubble contact area with the surface. The geometry is defined by h, the bubble height; r_b, the radius of curvature; a, the radius of the contact area with the surface; and θ, the contact angle of the liquid with the surface. By the application of voltage to the external electrodes, the contact area of the bubble with the surface decreases.

particles remotely.[25,26] In all of these studies, the translational motion of the surface-bound bubbles is achieved by the sequential actuation of adjacent electrodes.[23,24,27]

First, we address the main question of whether rendering a nonpatterned surface slippery for bubbles in a controlled fashion is possible. In particular, we aim to define the conditions for which radial oscillations of a surface-bound bubble, caused by a change in surface wettability, transform into translational motion. The influence of voltage, and consequently the change in contact angle, on lateral translational motion is experimentally investigated and discussed in terms of excess of surface energy and contact angle hysteresis. In addition, the influence of the shape and frequency of the applied electrical signal on the dynamics of the bubble motion is studied. The scope of this study is to show for the first time how the application of a deterministic force can lead to a stochastic motion of bubbles, which can be used for controlled bubble locomotion, coalescence, and possibly detachment from the surface.

Here we apply rectangular electrical pulses to an electrowettable surface decorated with micometer-sized bubbles. By careful tuning of the applied electric pulse and therefore by changing the contact area of the bubble with the surface, it is demonstrated that translational motion can be not only actuated but also regulated. If the periodicity of the actuation pulse is low, then there is enough time for the relaxation of the bubble without the resulting displacement. However, if the periodicity of the actuation pulse is set to a higher frequncy such that bubble oscillations are continuous, then an instability is induced, finally leading to translational motion.

RESULTS AND DISCUSSION

Catalytically Active Janus Nanodisks. Catalytically active Janus disks were used for the nucleation of microbubbles directly on the surface (Figure 1a). The disks are 6 μm in diameter and consist of 50-nm-thick Pt and Ni layers (each) on 200-nm-thick silicon nitride (Supporting Information). The platinum layer is catalytically active and is used as the bubble nucleation site through the splitting of H_2O_2 into H_2O and O_2. As the nanodisks are randomly distributed, the Pt side can be directly in contact with the surface or roughly 250 nm away from it. Bubbles nucleating on particles adjacent to a hydrophobic substrate spontaneously adhere to the surface, as was previously shown.[28]

Electrowetting of Bubbles. A chamber consisting of upper and bottom indium tin oxide (ITO) electrodes was used for the electrowetting experiments as seen in Figure 1b. A layer of polypropylene (PP) film was put on the bottom electrode. To ensure good contact between the PP film and the ITO layer, a thin liquid layer of aqueous KCl (0.5 M) was placed in between. In each experiment, an aqueous droplet containing the Janus disks is placed on the polypropylene film, and H_2O_2 (Experimental Section) is added in order to nucleate bubbles. The influence of the applied voltage on the bubble is shown schematically in Figure 1c. The contact area of the bubble with the surface decreases upon applying a voltage, as the contact angle (CA) drops. The disk thickness is on the nanometer scale; therefore, the bubbles easily adhere to the hydrophobic surface.[28] Below saturation, the contact angle θ_V follows the external voltage V according to the Young–Lippmann equation presented in eq 1.[29,30]
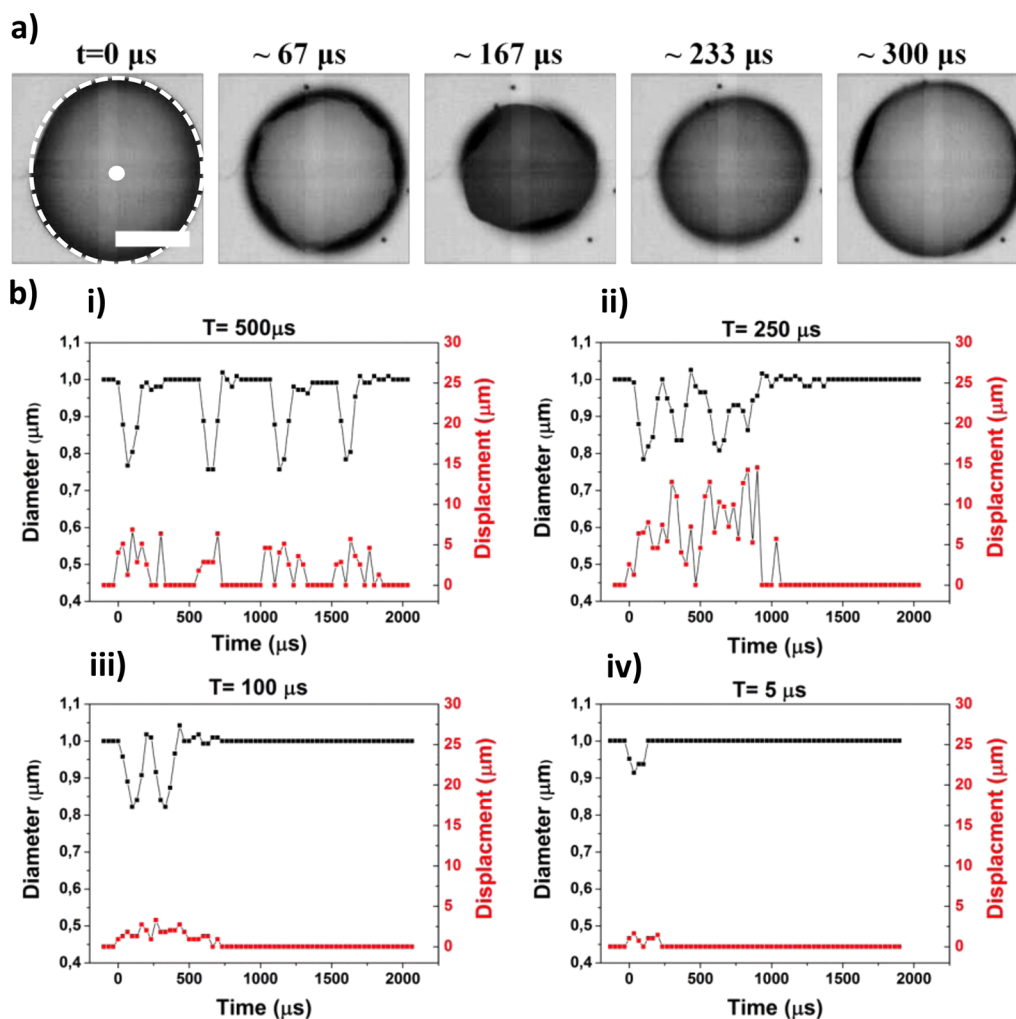
Figure 2. Time resolved optical microscopy of bubble radial oscillations on the surface. (a) Optical micrographs showing a bubble contraction−expansion cycle as a result of electrowetting for $T = 250~\mu s$. The bubble diameter and center were tracked on the basis of such image sets. The scale bar corresponds to $100~\mu m$. (b) Plots showing the diameter and displacement of bubbles subjected to four kinds of pulses: (i) $T = 500~\mu s$, (ii) $T = 250~\mu s$, (iii) $T = 100~\mu s$, and (iv) $T = 5~\mu s$.

$$\cos\theta_V = \cos\theta_o + \frac{\varepsilon_0\varepsilon_r V^2}{2\gamma_{LV}d} = \cos\theta_o + \frac{CV^2}{2\gamma_{LV}} = \cos\theta_o + \eta$$

(1)

γ_{LV} stands for the liquid/vapor interfacial tension, θ is the apparent contact angle, ε_o is the vacuum permittivity, ε_r is the specific permittivity, d is the thickness of the dielectric layer, C is the capacitance, and η is the electric component in electrowetting. The contact angle of the PP film without applied voltage was measured to be $\langle\theta_o\rangle = 103 \pm 2°$. The CA drops to $75 \pm 2°$ when a voltage of 300 V is applied (Figure S1 in the Supporting Information). In addition, the dynamic advancing and receding contact angles of a water droplet on the PP film without an applied voltage (in a sessile drop configuration) are $\langle\theta_a\rangle = 103 \pm 3$ and $\langle\theta_r\rangle~71 \pm 3°$, respectively.

Time-Resolved Tracking of Bubbles under Electrowetting. First, we investigate the transient response of single bubbles to different pulses. To understand the influence of the pulse periodicity on the bubble oscillations, a fast camera was used (30 000 fps or 33.3 μs per frame) together with optical microscopy to resolve the electrowetting behavior in real time and to estimate the distance a bubble travels over the course of

one pulse cycle. Using image analysis, we tracked the bubble diameter and position under the application of pulses of different amplitudes and widths. We denote T_p and T_n as the time periods of the positive and negative square pulses, respectively (Figure S3 in the Supporting Information). T_i is the time interval between the positive and negative pulses. In all experiments, we consider the symmetric case of $T = T_p = T_n = T_i$. P_s is the time between two subsequent pulse cycles and is considerably larger than T, thus the induced motion in one cycle is independent of the next cycle. Measurements of the bubble diameter and center of mass were extracted from the time-resolved optical micrographs as seen in Figure 2. The optical micrographs showing a contraction−expansion cycle of a bubble are presented in Figure 2a. (Full micrograph sequences can be found in the Supporting Information, Figure S4.) Such an image set enables intimate tracking of the bubble diameter and displacement during an electrowetting pulse (Figure 2b). The plots present the tracking of bubbles under four kinds of electric pulses: (i) $T = 500~\mu s$, (ii) $T = 250~\mu s$, (iii) $T = 100~\mu s$, and (iv) $T = 5~\mu s$, with $V = 300$ V in all cases. The initial diameters of these bubbles are 165, 185, 187, and 214 μm, respectively. Please note that the bubble diameter was measured using circle fitting. In some cases, there were
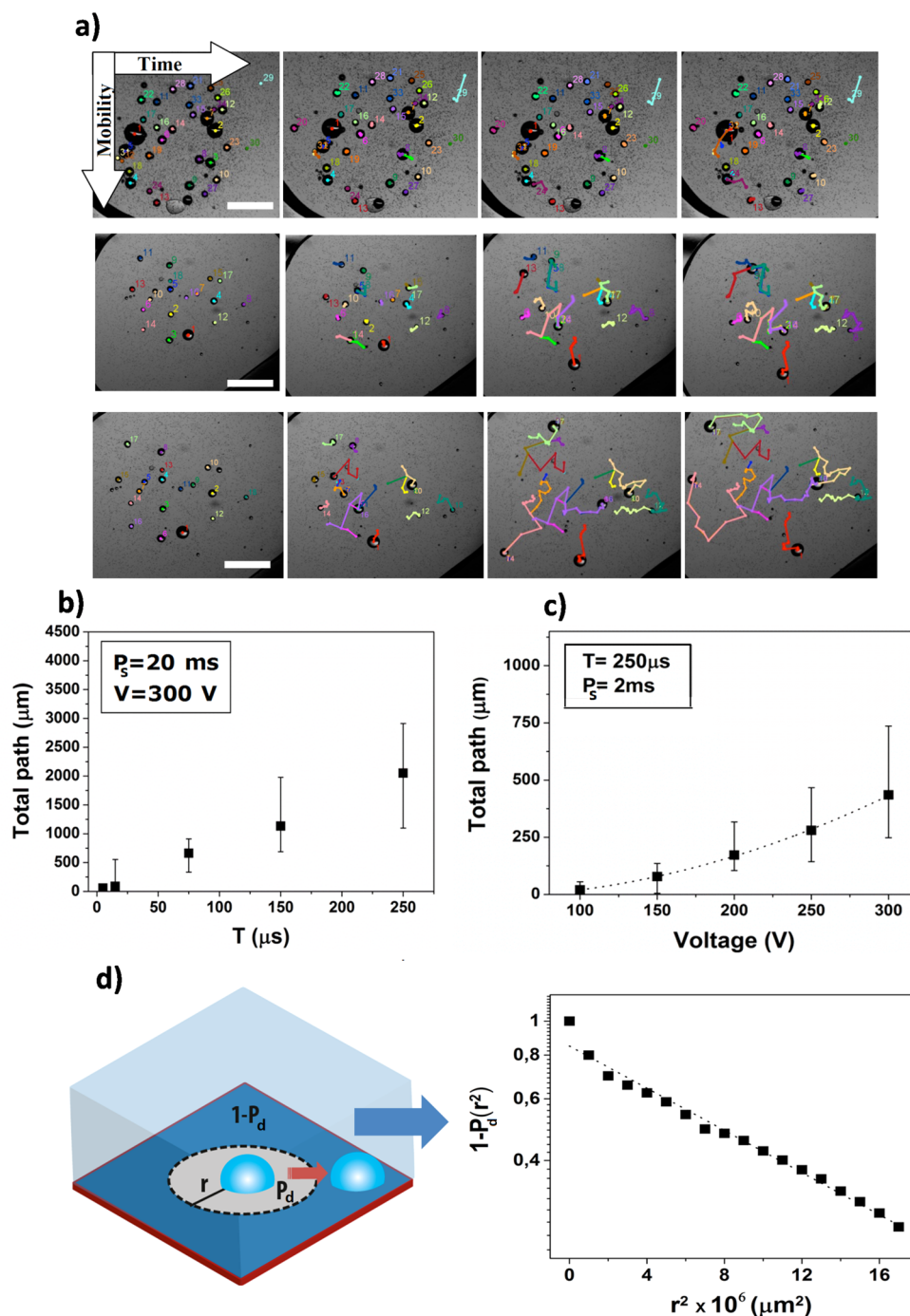
Figure 3. Bubble translational motion depending on signal periodicity and voltage. (a) Optical micrographs showing the displacement of bubbles tracked along 5500 successive pulse cycles. Each bubble is marked with a different color. The tracks were used to calculate the mean traveling path of bubbles under different conditions. The scale bar corresponds to 1 mm. Plots presenting the statistics of the total traveling path of bubbles depending (b) on the oscillation periodicity for pulses with $T = 5$, 15, 75, 150, and 250 μs and $P_s = 20$ ms and (c) on the voltage for a pulse of $T = 250$ μs and $P = 2$ ms. For the statistics, 500 successive pulse cycles were considered. (d) Probability distribution $1 - P_d(r^2)$ with a fit to eq 3.

deviations from a perfect circle due to the pinning of the contact line, and thus an error of up to 5 μm was measured. The presented diameters are normalized to their initial values in order to compare the bubble contraction in all cases. As seen in Figure 2b(i), the bubble contraction starts with the voltage pulse; however, it does not stay constant during the plateau of the pulse. We attribute the lack of a static change in contact angle to the symmetric ITO electrode setup. When the top electrode is replaced with a platinum electrode (which has a

much greater ability to supply current to the system), the measurement of the contact angle against the external voltage clearly shows a static response (Figure S1). We note that the rise time of the voltage (from 0 to the maximal voltage) is much longer in the measurement summarized in Figure S1 in the appendix (DC voltage) in comparison to that time in the case of the square pulse. Considering the diffusion constant of the ions in the bulk water on the order of 10^{-5} cm^2/s and the electrode distance of 1 mm, we find relaxation times for the

charge carriers in the bulk medium on the order of microseconds (equation S2 in the Supporting Information).[31] We can therefore assume that during the voltage rise the ITO-PP film-ITO system is not relaxed and the charges necessary for the electrowetting effect are supplied by a transient polarization current. After reaching the plateau, the system is quickly equilibrated to a state where apparently the PP film is uncharged. In other words, the voltage drops elsewhere in the system, likely on the large ITO−electrolyte interface impedance. This means that effectively the derivative of the applied pulse is the stimulus for the bubble. Although it is beyond the scope of this work to study this effect further, we focus on the instabilities of the bubbles induced by these transient processes. In Figure 2b(iv), the pulse with the shortest period $T = 5$ μs is shown. Here the bubble is limited by its dynamic response to the pulse, as can be seen by the negligible contraction. When the pulse width is increased, we find that the bubble contraction−expansion cycles relax with a characteristic time of approximately $T_r = 250$ μs, independent of the pulse width. Hence, this is considered to be the characteristic time of the bubble radial oscillations. It is now interesting to explore the effect of the pulse period T on the relaxation time. Although only a small displacement during the contraction cycle is recorded for both $T = 500$ μs $> T_r$ and $T = 5$ μs, 100 μs $< T_r$, a maximal displacement of as large as 14 μm is recorded for $T = 250$ μs $\approx T_r$. Furthermore, we point out that the displacement of the bubble center of mass during the oscillation differs from the final displacement at the end of the cycle. It is also interesting that changes in polarity do not affect the bubble response to electrowetting, as seen in the plots in Figure 2b. Considering that the CA of the surface in the absence of applied voltage is $\langle\theta_o\rangle = 103 \pm 2°$ and the bubble contracts to 75% of its original diameter in cases (i) and (ii), one can estimate the final CA of the surface from the geometry of the bubble using the illustration in Figure 1c. According to these geometrical considerations, the final diameter of the bubble corresponds to a CA of ∼77°, in agreement with the independent measurements of the electrowetting curve (Figure S1 in the Supporting Information) and in agreement with the argument above in which we witness a transient but complete electrowetting response during the fast voltage rise. Contact angles corresponding to contractions down to 80, 85, and 90% of the bubbles' original diameter were calculated as well and resulted in CA of ∼83, 88, and 92°, respectively. To study the bubble displacement further, we measured the macroscopic path traveled by the bubbles over many pulse cycles.

Bubble Dance: Regulating Bubble Mobility by Tuning Electrowetting Periodicity. Now we applied a series of 500 pulse cycles of duration T. Consistent with the previous single-pulse experiments, we find that tuning the pulse width influences the macroscopic path the bubbles travel. The tracking of bubble motion under electrowetting with varying parameters is presented in Figure 3. The average traveling distance was calculated along 500 pulse cycles, and the statistics are based on analyzing the tracks of at least 15 bubbles per configuration. The bubble catalytic growth is much slower than the time scale of the applied voltage; therefore, the bubble volume is presumed to be constant during the experiment. Detached bubbles accumulate at the top of the chamber and exhibit neither oscillations nor translational motion. Thus, the bubbles are not influenced by Maxwell stresses caused by the transient electric field directly but rather by the change in the

surface wettability, as formulated in the Young−Lippmann equation.

Figure 3a presents optical micrographs extracted from videos recorded at 2 fps (or 500 ms per frame). One can clearly see the differences between the mobility of the bubbles for different pulse settings. For very short electrowetting pulses ($T = 5$, 10 μs), the bubbles do not perform full oscillations; therefore, their displacement is hindered whereas continuous full contraction−expansion cycles result in large displacements as seen in the latter cases ($T = 75$, 150, and 250 μs). A careful adjustment of the oscillations is the key point for tuning the bubble mobility. The influence of the pulse periodicity on the bubble displacement is summarized in Figure 3b for pulses of $T = 5$, 15, 75, 150, and 250 μs with $P_s = 20$ ms. In these experiments, the voltage amplitude was set to 300 V. As was previously discussed, a complete oscillation cycle lasts roughly 250 μs (Figure 2b). When adjusting the periodicity of the oscillations so that a bubble is under a continuous transitional state of changing its contact area with the surface, bubbles start showing a significant enhancement in translational motion. The maximal traveling path over 500 pulses can reach almost 3000 μm, which is 1 to 2 orders of magnitude higher than the bubbles dimensions. It is inferred from Figure 2 that the displacement of bubbles takes place only during the bubble contraction−expansion cycle. Therefore, the value of P_s (the time interval between pulses) does not influence the magnitude of the traveling path.

Bubble Random Walk Underwater. Now we link the traveling path along one pulse cycle, as seen in Figure 2, to the macrodisplacement, as seen in Figure 3a. We consider the model of a random walk with the traveled end-to-end distance R and displacement r for N steps with a displacement, or jump, of a (eq 2).[32]

$$R = \sqrt{\overline{r^2}} = a\sqrt{N} \tag{2}$$

Over the course of 500 ms (video resolution), many oscillation and displacement cycles take place ($T = 250$ μs). In the limit of continuity considered here, the squared distance from the origin r^2 in a random walk model follows the probability distribution in eq 3.[33]

$$P_d(r^2, t) = 1 - \exp\left(\frac{r^2}{r(t)_0{}^2}\right) \tag{3}$$

P_d is the probability of finding a bubble a distance equal to or smaller than r^2 after a number of steps or time t. From the acquired movies, we could track and extract the bubble path and calculate the corresponding probability distribution. We counted the number of bubbles, which were within a circle of radius r from their starting point for a fixed time t. To normalize, the distribution is scaled by the total number of points. A total of 18 bubbles over the time course of 10 s were considered. The calculated probability distribution along with the fit to eq 3 is shown in Figure 3d (note the logarithmic scale). We obtain remarkable agreement for small to intermediate distances. We conclude that the bubbles indeed follow a random walk. Over longer distances, bubbles coalesce and thus cannot be considered. We note that a wide range of bubble sizes (approximately 80−500 μm in diameter and 240 μm on average) was considered in the analysis, yet we obtain a good fit ($R^2 = 0.982$) to a one-population model. We conclude that for the bubble sizes considered the jump distance a does not depend strongly on the size of the bubble. This can be

understood from an energy balance for a single bubble displacement shown in eq 4

$$\int d\vec{s}\ \vec{F}_{drag} = \frac{\pi r_b^2 C}{2V^2} \tag{4}$$

where F_{drag} is the drag force, r_b is the radius of the bubble, and C is the PP film capacitance per unit area, which can be deduced from eq 1. For the condition in which the kinetic movement dominates the relaxation by oscillations and under the assumption of a steady state during small linear displacements a, we find

$$a \propto \frac{r_b^2 C}{F_{drag}} V^2 \tag{5}$$

Neglecting contact line effects, F_{drag} will be dominated by the fluid drag force and hence will roughly scale as r^2. Hence the distance of the displacement per jump will not depend on the bubble size. This confirms the previous analysis using eq 3. Finally, we test the dependence of the total traveling path of the bubbles on the voltage (Figure 3c). The cumulative total path under each voltage was measured over N = 500 pulse cycles. Assuming the jump distance per one pulse, a, is constant, the total path the bubbles travel in each experiment is 500 times a. Considering 5 the total traveling path is proportional to V^2. We find good agreement between this simple theory and data for the intermediate set of voltages. For voltages of 100 V and below, bubble total traveling path is minor. In this range, the change in CA is roughly 10°. However, when the voltage exceeds 200 V the CA drops to approximately 75°, and considerably larger travel distances are observed. Although saturation of the contact angle was measured above 200 V, it can be inferred from the plot that displacement continues to increase from roughly 200 μm to more than 500 μm (mean values) with voltage in the range of 200−300 V. It is important to remember that the electric component in the Young−Lippmann equation, which represents the electric contribution in terms of electric force (or energy) acting on the contact line, scales with the square voltage. Hence, it is possible that the electric force continues to increase in this voltage range and can further induce displacement while the CA remains saturated.

System Model for Bubble Translational Motion. To estimate the contribution of the incomplete relaxation of the bubble to its translational motion, the energy of a bubble during a contraction cycle is considered. This energy was calculated using the terms shown in Figure 4. Two states are taken into account: (a) the initial/final states corresponding to CA = 103° and (b) a fully contracted bubble under a voltage of 300 V, corresponding to CA = 75°. Before a bubble is subjected to a voltage in an electrowetting experiment, its initial surface energy E_i is given by

$$E_i = A_i \gamma_{SV} + S_i \gamma_{LV} \tag{6}$$

A is the contact area of the bubble with the surface, S is the surface area of the spherical cup. Under the applied voltage, the surface energy E_f is given by

$$E_f = A_f \gamma_{SV} + (A_i - A_f)\gamma_{SL} + S_f \gamma_{LV} \tag{7}$$

Finally, when the voltage is no longer applied, the bubble energy is described again by E_i. As was previously discussed, the translational motion of the bubble is observed when contraction starts to take place. Considering the time resolution of 33.3 μs per frame, it is possible to estimate the velocity of a
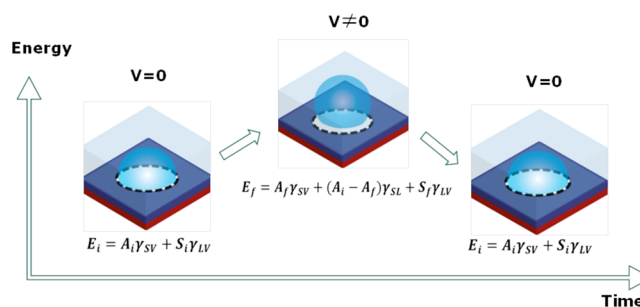
Figure 4. Energy of a bubble during a contraction−expansion cycle. Illustration presenting a bubble attached to a surface of different contact angles and their corresponding energies (bottom). (a) Initial state on a hydrophobic substrate (CA > 90 °). (b) Final state on a hydrophilic substrate (CA < 90 °), corresponding to a substrate under an applied voltage. The volume of the bubble remains constant.

bubble during a pulse. Analyzing the bubble displacement based on the plot in Figure 2b(ii) (for a pulse of T = 250 μs), the displacement of the bubble when contraction starts is approximately 100 nm. However, when the bubble diameter does not fully recover before another contraction takes place ($t \approx 750\ \mu$s in Figure 2b(ii)) an additional mobility is induced. In this case, a displacement of roughly 0.5 μm, which is ~5 times the displacement of the in-place oscillations, is recorded.

According to energy calculations, the maximal energy difference between the two states is roughly 10^{-10} J for a bubble with an initial diameter of 165 μm. The values used for the calculations are γ_{LV} = 72 mN/m and γ_{SV} = 30 mN/m for the polypropylene film.[34] Clearly this is the upper limit in energy difference between the two states. The Reynold's number in the system is approximately 10 (Supporting Information), and thus this excess surface energy can be related to the kinetic energy. Nevertheless, the actual fraction of energy potentially transformed to kinetic energy is much smaller, considering drag forces and heating. Additionally, the contact line of the bubble with the surface is subjected to pinning, decreasing its mobility. An example of an incomplete radial oscillation can be seen in Figure 2b(ii). Such an oscillation corresponds in theory to an energy difference of 0.5 $\times\ 10^{-10}$ J. In terms of kinetic energy, this corresponds to a velocity of 7 μm/μs. From the plot, it can be inferred that the bubble displacement at $t \approx 750\ \mu$s is roughly 15 μm (measured between two consecutive frames). Therefore, the velocity of the bubble is approximately 0.5 μm/μs. As expected, the real velocity of the bubble is much smaller than the theoretical value considering that the bubble needs to overcome the surface adhesion force, local pinning, and shear forces acting on the contact line during the radial oscillation.[35,36]

Finally, we want to comment on the origin of the bubbles lateral movement. The displacement of the bubble has to be driven by a gradient in surface energy because the applied field is normal to the surface. In principle, the displacement of a bubble is possible if the change in the contact angle of the substrate, on which the bubble is situated, exceeds the range of the contact angle hysteresis. In other words, the contact angle hysteresis can be treated as the solid−liquid adhesive force, and in overcoming this adhesion, it is possible to actuate translational motion.[24,37] When droplets are discussed, two competitive mechanisms that can describe the behavior of metastable states on a smooth heterogeneous surface were previously suggested.[38] In the first, a droplet tends to remain in

its asymmetric state, whereas energy is being reduced by reshaping, for example. In the second mechanism, the metastability is a driving force for the droplet to move toward a position in which its energy is reduced. In the case of bubbles, several parallel mechanisms can be responsible for translational motion. Local pinning due to the surface roughness of the dielectric substrate or the presence of the nanodisks causes the bubble center to dislocate, as seen in Figure S5 in the Supporting Information. For the same reason, the electrical component acting parallel to the surface is not symmetric. Finally, if the bubble lacks sufficient time to reorient, following the instantaneous change in the contact angle, then an additional instability is introduced. The energy of the bubble in this metastable state can be reduced if the bubble changes its position. These mechanisms are acting in parallel; however, only the last one can explain the striking differences in bubble response to pulsed voltage.

Comparison between Bubble Use in Nature and the Artificial Actuation of Bubbles for Underwater Locomotion. Insects, specifically terrestrial beetles, capable of walking underwater by using entrapped bubbles in their legs, were first reported by Hosoda et al.[1] The mechanism of locomotion on solid surfaces underwater is a combination of hydrophobic effects, enforced attachment, and the detachment of bubbles from the surface and capillary forces. Traction forces generated by the leaf beetle on hydrophobic surfaces range between 3 and 8 mN. This translates to work in the range of a few dozen nJ for distances on the micrometer scale. Considering eqs 6 and 7 in this study, the work performed by electrowetting on a surface-anchored bubble of 165 μm diameter is approximately 0.1 nJ, smaller than what is observed in nature. However, this is logical considering some fundamental differences between the two cases. First, the bubbles used by insects are entrapped in a setal structure that stabilizes them in comparison to the bubbles in this study, which are anchored to the surface only. As a result, these two systems differ geometrically. Additionally, the contact area of the beetle tarsomere with the surface is roughly 300 μm in width and 150 μm in length,[39] and we consider a smaller round bubble of 165 μm diameter for the energy calculations. Finally, it is important to remember that although traction forces were previously measured, the beetles actually use reversible attachment and detachment from the surface using air bubbles to perform underwater locomotion.

Actuated Functionalities Induced by Mobility. We have established how and under which conditions bubbles can be actuated to move across an unpatterned surface. Now we show that bubble mobility on the surface can be used to fulfill a variety of tasks.[24,40−42] A crucial problem when using microfluidic devices is clogging by bubbles or by contaminants. Here it is suggested that the actuated motion of bubbles can be used to clean and unblock microchannels. Figure 5 shows how the mobility of bubbles on the surface could be beneficial to performing a variety of functions at the solid/water interface. Mobility is demonstrated to be useful for coalescence, trapping, carrying cargo, and bubble transport. The coalescence of adjacent bubbles is shown in Figure 5a. This depends on the mobility and distribution of the bubbles. According to Figure 4, the coalescence of microbubbles within the range of millimeters is possible upon adjustment of the electrowetting pulse. This range is attractive for microfluidic devices in which the channels are usually smaller than this order of magnitude. In addition, the trapping of bubbles is possible if traps are in the vicinity of mobile bubbles. In Figure 5b, it is shown that a bubble is
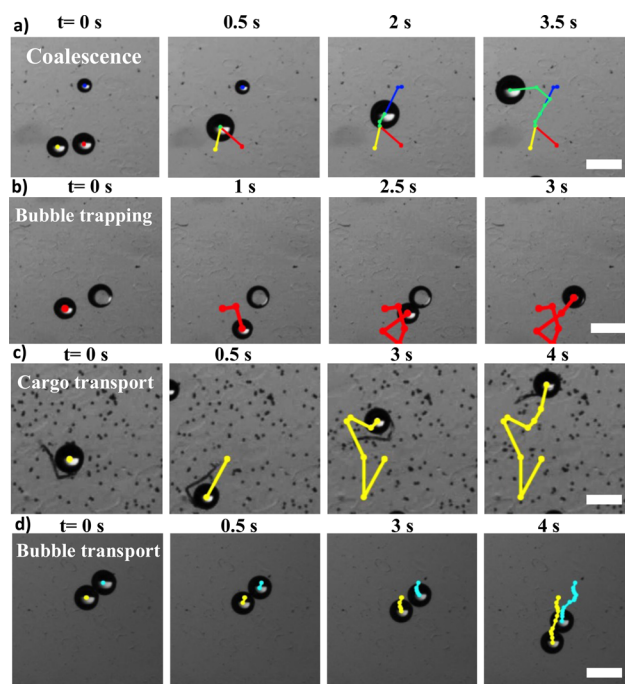
Figure 5. Functions induced by bubble translational motion: (a) coalescence, (b) trapping, (c) cargo transport, and (d) bubble transport. The scale bar corresponds to 200 μm.

trapped in a circularly shaped island that is not subjected to electrowetting. The electrowetting setup used in this study uses a thin conductive layer between the electrode and the dielectric PP layer. In an area where the conductive aqueous medium is absent, bubbles are no longer subjected to electrowetting, and thus once a bubble reaches a trap, it is fixed there. Upon locating these traps in known positions, one can guide and predetermine the final position of the microbubbles. As more bubbles come close to this trap, they coalesce to form larger bubbles, which eventually have to detach under buoyancy forces. In Figure 5c, one can see contamination carried by a bubble along its path. The dark spheres are polystyrene microparticles (16 μm). As seen in the image sequence and in accordance with previous studies, the small particles are not being trapped, contrary to the greater degree of contamination. Finally, adjacent bubbles are able to attract each other because of secondary Bjerknes forces.[43] In Figure 5d, one can see a bubble pair traveling together as a result of Bjerknes attractive forces.

■ CONCLUSIONS

In this study, the underwater locomotion of surface-anchored bubbles is actuated by electrowetting. It is shown that by the proper tuning of voltage periodicity a bubble instability can be induced, promoting translational motion of up to 2 orders of magnitude greater than the bubble size. Time-resolved (μs) imaging suggests that there is a threshold above which the translational motion of surface-anchored bubbles is preferred over radial oscillations. The translational motion fits a random walk model so that the hydrophobic surface becomes "slippery" for bubbles. The voltage in terms of amplitude and frequency dictates the degree of mobility of the bubbles and is a key tool in regulating their motion. The excess interfacial energy of a bubble in the course of one contraction−expansion cycle is calculated in order to estimate its contribution to the

translational movement on the surface. The calculated energies are compared to previous studies dealing with underwater locomotion via bubble use as performed by several insects in nature. Finally, additional outcomes of bubble mobility on the surface are demonstrated: actuated coalescence, trapping, and cargo transport. The actuated motion of bubbles on hydrophobic surfaces could be of great interest for applications in the fields of underwater adhesion, underwater cleaning mechanisms, microfluidics, and lab-on-a-chip devices in wet environments. An outlook of this work envisions directing the motion of bubbles inside microfluidic channels and the actuated motion of bubbles along wettability gradients to induce directionality in the motion, crucial to the applicability of these findings. Another interesting aspect is the dynamic response of bubbles to electrowetting using electric waves of different shapes and surfaces with hierarchical structures.[44,45] Such surfaces might be suitable for inducing the transition between lateral mobility and the controlled detachment of bubbles from the surface.[46] Finally, an interesting aspect yet to be explored is the response of bubbles of smaller dimensions (nanobubbles) to electrowetting on hydrophobic surfaces.[47,48]

■ EXPERIMENTAL SECTION

Chemicals. A 4-μm-thick polypropylene film was provided by Goodfellows GmbH. H_2O_2 (30%) and KCl were provided by Sigma-Aldrich. Polystyrene beads (16 μm in diameter) were provided by Microparticles GmbH.

Instrumentation. A Zeiss (Axiovert 135TV, Germany) microscope was used for time-resolved optical imaging. Time-resolved imaging was carried out with a fast digital camera (HG-100 K, Redlake Inc., San Diego, CA). A Leica (M165C) microscope was used for optical imaging. Images were analyzed by ImageJ, and Matlab R2014a was used for calculations.

Experiment. In each experiment, 10 μL of KCl (0.5 M) was spread between the ITO-covered glass and the PP film. A droplet containing 20 μL of a nanodisk suspension, 5 μL of KCl (0.5 M), and 20 μL of distilled water was spread on the PP film, followed by the addition of 5 μL of H_2O_2 (20% in distilled water). The conductivity of 10% v/v KCl (0.5 M) in distilled water was measured to be 5.23 mS/cm.

■ ASSOCIATED CONTENT

ⓢ Supporting Information

The Supporting Information is available free of charge on the ACS Publications website at DOI: 10.1021/acs.langmuir.5b03821.

Single bubbles perform radial oscillations under different pulse parameters (U = 300V, T = 5 μs) (AVI)

Single bubbles perform radial oscillations under different pulse parameters (U = 300 V, T = 100 μs) (AVI)

Single bubbles perform radial oscillations under different pulse parameters (U = 300 V, T = 250 μs) (AVI)

Single bubbles perform radial oscillations under different pulse parameters (U = 300 V, T = 500 μs) (AVI)

Bubble tracking used for statistics and verification of the random walk model (U_p = 100 V, T = 250 μs tracks) (AVI)

Bubble tracking used for statistics and verification of the random walk model (U_p = 200 V, T = 250 μs tracks) (AVI)

Bubble tracking used for statistics and verification of the random walk model (U_p = 300 V, T = 250 μs tracks) (AVI)

Bubble tracking used for statistics and verification of the random walk model (U_p = 300 V, T = 250 μs tracks) (AVI)

Bubble trapping (AVI)

Bubble carrying cargo (AVI)

Bubble pair motion (AVI)

List of movie parameters. Young−Lippmann equation. Einstein's equation for active diffusion in an electric field. Energy considerations. Reynolds number equation. Electrowetting curve of polypropylene. Morphology of the polypropylene film. The electric signal. Time-resolved electrowetting of bubbles. Janus nanodisk synthesis. (PDF)

■ AUTHOR INFORMATION

Corresponding Author
*E-mail: batel.pinchasik@mpikg.mpg.de.

Notes
The authors declare no competing financial interest.

■ REFERENCES

(1) Hosoda, N.; Gorb, S. N. Underwater Locomotion in a Terrestrial Beetle: Combination of Surface de-Wetting and Capillary Forces. *Proc. R. Soc. London, Ser. B* **2012**, *279* (1745), 4236−4242.

(2) Barthlott, W.; Neinhuis, C. Purity of the Sacred Lotus, or Escape from Contamination in Biological Surfaces. *Planta* **1997**, *202* (1), 1−8.

(3) Marmur, A. The Lotus Effect: Superhydrophobicity and Metastability. *Langmuir* **2004**, *20* (9), 3517−3519.

(4) Ling, W. Y. L.; Lu, G.; Ng, T. W. Increased Stability and Size of a Bubble on a Superhydrophobic Surface. *Langmuir* **2011**, *27* (7), 3233−3237.

(5) Wong, W. S. Y.; Nasiri, N.; Liu, G.; Rumsey-Hill, N.; Craig, V. S. J.; Nisbet, D. R.; Tricoli, A. Flexible Transparent Hierarchical Nanomesh for Rose Petal-Like Droplet Manipulation and Lossless Transfer. *Adv. Mater. Interfaces* **2015**, *2*, 1500071.

(6) Feng, L.; Li, S.; Li, Y.; Li, H.; Zhang, L.; Zhai, J.; Song, Y.; Liu, B.; Jiang, L.; Zhu, D. Super-Hydrophobic Surfaces: From Natural to Artificial. *Adv. Mater.* **2002**, *14* (24), 1857−1860.

(7) Jiang, L.; Zhao, Y.; Zhai, J. A Lotus-Leaf-like Superhydrophobic Surface: A Porous Microsphere/Nanofiber Composite Film Prepared by Electrohydrodynamics. *Angew. Chem.* **2004**, *116* (33), 4438−4441.

(8) Zhang, L.; Wu, J.; Wang, Y.; Long, Y.; Zhao, N.; Xu, J. Combination of Bioinspiration: A General Route to Superhydrophobic Particles. *J. Am. Chem. Soc.* **2012**, *134*, 9879−9881.

(9) Yu, J.; Chen, H.; Liu, Y.; Craig, V. S. J.; Wang, C.; Li, L. H.; Chen, Y. Superhydrophobic and Superoleophilic Porous Boron Nitride Nanosheet/Polyvinylidene Fluoride Composite Material for Oil-Polluted Water Cleanup. *Adv. Mater. Interfaces* **2015**, *2*, 1400267/1− 1400267/10.

(10) Rykaczewski, K.; Paxson, A. T.; Anand, S.; Chen, X.; Wang, Z.; Varanasi, K. K. Multimode Multidrop Serial Coalescence Effects during Condensation on Hierarchical Superhydrophobic Surfaces. *Langmuir* **2013**, *29* (3), 881−891.

(11) Li, H.; Zheng, M.; Liu, S.; Ma, L.; Zhu, C.; Xiong, Z. Reversible Surface Wettability Transition between Superhydrophobicity and Superhydrophilicity on Hierarchical Micro/nanostructure ZnO Mesh Films. *Surf. Coat. Technol.* **2013**, *224*, 88−92.

(12) Lim, H. S.; Kwak, D.; Lee, D. Y.; Lee, S. G.; Cho, K. UV-Driven Reversible Switching of a Roselike Vanadium Oxide Film between Superhydrophobicity and Superhydrophilicity. *J. Am. Chem. Soc.* **2007**, *129* (14), 4128−4129.

(13) Xu, Z.; Ao, Z.; Chu, D.; Younis, A.; Li, C. M.; Li, S. Reversible Hydrophobic to Hydrophilic Transition in Graphene via Water Splitting Induced by UV Irradiation. *Sci. Rep.* **2014**, *4*, 6450.

(14) Jiang, Q. G.; Ao, Z. M.; Chu, D. W.; Jiang, Q. Reversible Transition of Graphene from Hydrophobic to Hydrophilic in the

Presence of an Electric Field. *J. Phys. Chem. C* **2012**, *116* (36), 19321−19326.

(15) Klarman, D.; Andelman, D.; Urbakh, M. A Model of Electrowetting, Reversed Electrowetting, and Contact Angle Saturation. *Langmuir* **2011**, *27*, 6031−6041.

(16) Chen, L.; Bonaccurso, E. Electrowetting - From Statics to Dynamics. *Adv. Colloid Interface Sci.* **2014**, *210*, 2−12.

(17) Jun Lee, S.; Lee, S.; Hyoung Kang, K. Droplet Jumping by Electrowetting and Its Application to the Three-Dimensional Digital Microfluidics. *Appl. Phys. Lett.* **2012**, *100*, 081604/1−081604/3.

(18) Lee, S.; Lee, S.; Kang, K. Jumping of a Droplet on a Superhydrophobic Surface in AC Electrowetting. *J. Visualization* **2011**, *14* (3), 259−264.

(19) Lapierre, F.; Coffinier, Y.; Boukherroub, R.; Thomy, V. Electro-(de)wetting on Superhydrophobic Surfaces. *Langmuir* **2013**, *29* (44), 13346−13351.

(20) Li, F.; Mugele, F. How to Make Sticky Surfaces Slippery: Contact Angle Hysteresis in Electrowetting with Alternating Voltage. *Appl. Phys. Lett.* **2008**, *92*, 244108/1−244108/3.

(21) Lee, S. J.; Hong, J.; Kang, K. H.; Kang, I. S.; Lee, S. J. Electrowetting-Induced Droplet Detachment from Hydrophobic Surfaces. *Langmuir* **2014**, *30* (7), 1805−1811.

(22) Chung, S.; Rhee, K.; Cho, S. Bubble Actuation by Electrowetting-on-Dielectric (EWOD) and Its Applications: A Review. *Int. J. Precis. Eng. Manuf.* **2010**, *11* (6), 991−1006.

(23) Chung, S. K.; Kwon Cho, S. On-Chip Manipulation of Objects Using Mobile Oscillating Bubbles. *J. Micromech. Microeng.* **2008**, *18* (12), 125024.

(24) Zhao, Y.; Cho, S. K. Micro Air Bubble Manipulation by Electrowetting on Dielectric (EWOD): Transporting, Splitting, Merging and Eliminating of Bubbles. *Lab Chip* **2007**, *7* (2), 273−280.

(25) Chung, S. K.; Cho, S. K. Capturing, Carrying, and Releasing of Micro-Objects by AC-Electroweting-Actuated Oscillating Bubbles. *Solid-State Sens. Actuators Microsyst. IEEE Int. Conf.* **2009**, 821−824.

(26) Chung, S. K.; Zhao, Y.; Yi, U. C.; Cho, S. K. Micro Bubble Fluidics by EWOD and Ultrasonic Excitation for Micro Bubble Tweezers. *Micro Electro Mech. Syst. IEEE 20th Int. Conf.* **2007**, 31−34.

(27) Chung, S. K.; Kwon, J. O.; Cho, S. K. Manipulation of Micro/Mini-Objects by AC-Electrowetting-Actuated Oscillating Bubbles: Capturing, Carrying and Releasing. *J. Adhes. Sci. Technol.* **2012**, *26* (12−17), 1965−1983.

(28) Pinchasik, B.-E.; Möhwald, H.; Skirtach, A. G. Mimicking Bubble Use in Nature: Propulsion of Janus Particles due to Hydrophobic-Hydrophilic Interactions. *Small* **2014**, *10* (13), 2670−2677.

(29) Mugele, F. Fundamental Challenges in Electrowetting: From Equilibrium Shapes to Contact Angle Saturation and Drop Dynamics. *Soft Matter* **2009**, *5* (18), 3377−3384.

(30) Quinn, A.; Sedev, R.; Ralston, J. Contact Angle Saturation in Electrowetting. *J. Phys. Chem. B* **2005**, *109*, 6268−6275.

(31) Friedman, A. M.; Kennedy, J. W. The Self-Diffusion Coefficients of Potassium, Cesium, Iodide and Chloride Ions in Aqueous Solutions1. *J. Am. Chem. Soc.* **1955**, *77* (17), 4499−4501.

(32) Smidsrod, O.; Storker, T. M. *Biopolymer Chemistry* **2008**.

(33) Schütz, G. J.; Schindler, H.; Schmidt, T. Single-Molecule Microscopy on Model Membranes Reveals Anomalous Diffusion. *Biophys. J.* **1997**, *73* (2), 1073−1080.

(34) Lee, L.-H. Relationships between Surface Wettability and Glass Temperatures of High Polymers. *J. Appl. Polym. Sci.* **1968**, *12*, 719−730.

(35) Snoeijer, J. H.; Andreotti, B. Moving Contact Lines: Scales, Regimes, and Dynamical Transitions. *Annu. Rev. Fluid Mech.* **2013**, *45*, 269.

(36) Gao, L.; McCarthy, T. J. Contact Angle Hysteresis Explained. *Langmuir* **2006**, *22* (14), 6234−6237.

(37) Extrand, C. W. A Thermodynamic Model for Contact Angle Hysteresis. *J. Colloid Interface Sci.* **1998**, *207* (1), 11−19.

(38) Marmur, A. Contact Angle Hysteresis on Heterogeneous Smooth Surfaces. *J. Colloid Interface Sci.* **1994**, *168* (1), 40−46.

(39) Kokhuis, T. J. A.; Naaijkens, B. A.; Juffermans, L. J. M.; Kamp, O.; Versluis, M.; de Jong, N. Secondary Bjerknes Forces Deform Targeted Microbubbles. *Ultrason. Symp. IUS IEEE Int.* **2012**, 1−4.

(40) Marmottant, P.; Hilgenfeldt, S. Controlled Vesicle Deformation and Lysis by Single Oscillating Bubbles. *Nature* **2003**, *423* (6936), 153−156.

(41) Ko, S. H.; Lee, S. J.; Kang, K. H. A Synthetic Jet Produced by Electrowetting-Driven Bubble Oscillations in Aqueous Solution. *Appl. Phys. Lett.* **2009**, *94*, 194102/1−194102/3.

(42) Lee, J. H.; Lee, K. H.; Won, J. M.; Rhee, K.; Chung, S. K. Mobile Oscillating Bubble Actuated by AC-Electrowetting-on-Dielectric (EWOD) for Microfluidic Mixing Enhancement. *Sens. Actuators, A* **2012**, *182* (0), 153−162.

(43) Pelekasis, N. A.; Gaki, A.; Doinikov, A.; Tsamopoulos, J. A. Secondary Bjerknes Forces between Two Bubbles and the Phenomenon of Acoustic Streamers. *J. Fluid Mech.* **1999**, *500*, 313−347.

(44) Verho, T.; Korhonen, J. T.; Sainiemi, L.; Jokinen, V.; Bower, C.; Franze, K.; Franssila, S.; Andrew, P.; Ikkala, O.; Ras, R. H. A. Reversible Switching between Superhydrophobic States on a Hierarchically Structured Surface. *Proc. Natl. Acad. Sci. U. S. A.* **2012**, *109* (26), 10210−10213.

(45) Papadopoulou, E. L.; Barberoglou, M.; Zorba, V.; Manousaki, A.; Pagkozidis, A.; Stratakis, E.; Fotakis, C. Reversible Photoinduced Wettability Transition of Hierarchical ZnO Structures. *J. Phys. Chem. C* **2009**, *113* (7), 2891−2895.

(46) Barberoglou, M.; Zorba, V.; Pagozidis, A.; Fotakis, C.; Stratakis, E. Electrowetting Properties of Micro/Nanostructured Black Silicon. *Langmuir* **2010**, *26*, 13007−13014.

(47) Borkent, B. M.; Schoeherr, H.; Le Caee, G.; Dollet, B.; Lohse, D. Preferred Sizes and Ordering in Surface Nanobubble Populations. *Phys. Rev. E Stat. Nonlin. Soft Matter Phys.* **2009**, *80*, 036315/1−036315/4.

(48) Zhang, X. H.; Quinn, A.; Ducker, W. A. Nanobubbles at the Interface between Water and a Hydrophobic Solid. *Langmuir* **2008**, *24* (9), 4756−4764.

■ NOTE ADDED AFTER ASAP PUBLICATION

This paper was published on the Web on December 14, 2015, with errors in the Abstract text and in the sixth paragraph of the Results and Discussion section. The corrected version was reposted on December 15, 2015.